JATIS Journal of Astronomical Telescopes, Instruments, and Systems

RESEARCH PAPER

Spectrograph stabilization using a single-delay interferometer on the Hale Telescope

David J. Erskine,[a,*] Jerry Edelstein,[b] Edward H. Wishnow,[c] Martin M. Sirk,[c] Eric V. Linder,[b] and Dayne E. Fratanduono[a]

[a](Retired) Lawrence Livermore National Laboratory, Livermore, California, United States
[b]Lawrence Berkeley National Laboratory, Berkeley, California, United States
[c]University of California, Space Sciences Laboratory, Berkeley, California, United States

ABSTRACT. We describe a technique for spectrograph stabilization useful when conventional mitigation techniques of vacuum tanks, thermal insulation, and laser frequency comb may be impractical, expensive, heavy, or bulky. This includes spectrographs on airborne platforms or mounted on telescopes where they suffer a changing gravity vector or other drifts. Placing a fixed-delay interferometer in series with a spectrograph forms an externally dispersed interferometer (EDI). This produces a uniform sinusoidal comb multiplying input spectrum, creating (through heterodyning) beats (moiré patterns). In Fourier space for low frequencies up to the comb frequency, the moiré generated signal counter-rotates to ordinary spectra under an unknown disperser wavenumber drift Δx. This generates a large negative feedback signal useful in a conceptual control loop, to converge rapidly to a stable spectrum and yield Δx. A modified EDI data analysis algorithm ("crossfading") combines frequency-weighted moiré with conventional spectrum to cancel net output spectrum reaction to Δx. Needing only a single-delay, this is a practical improvement over prior crossfading analyses requiring multiple delays. We test crossfading on ThAr data near 4850 cm^{-1} taken on Hale telescope in an earlier project. In a single pass, we reduce drift 20 times. Using seven iterations, we reduce 0.5 cm^{-1} (31 km/s Doppler equivalent) drift to 4×10^{-7} cm^{-1} (2.5 cm/s). The interferometer delay can wander, because linearity of phase versus wavenumber interpolates science features between bracketing calibrating spectral references. Second, mathematically reversing the heterodyning effect doubles effective spectral resolution without changing disperser slit.

Keywords: high-resolution spectroscopy; spectrograph stabilization; Doppler radial velocimetry; exoplanet detection; externally dispersed interferometry; dispersed fixed delay interferometry; cosmic redshift drift

Paper 24080G received Jun. 4, 2024; revised Apr. 6, 2026; accepted Jun. 8, 2026; published Jun. 25, 2026.

1 Synopsis

1.1 Prior Work: Multiple Delay EDI on Hale Telescope

Dispersive spectrographs come in a wide variety of sizes and performance capabilities—used for a broad range of applications in science and engineering. In the 2007–2011 era, we performed experiments[1–3] at the Mt. Palomar Obs. 5 m Hale Telescope, testing externally dispersed interferometry (EDI) in conjunction with the TripleSpec[4] NIR spectrograph.

*Address all correspondence to David J. Erskine, derskine@spectralfringe.org

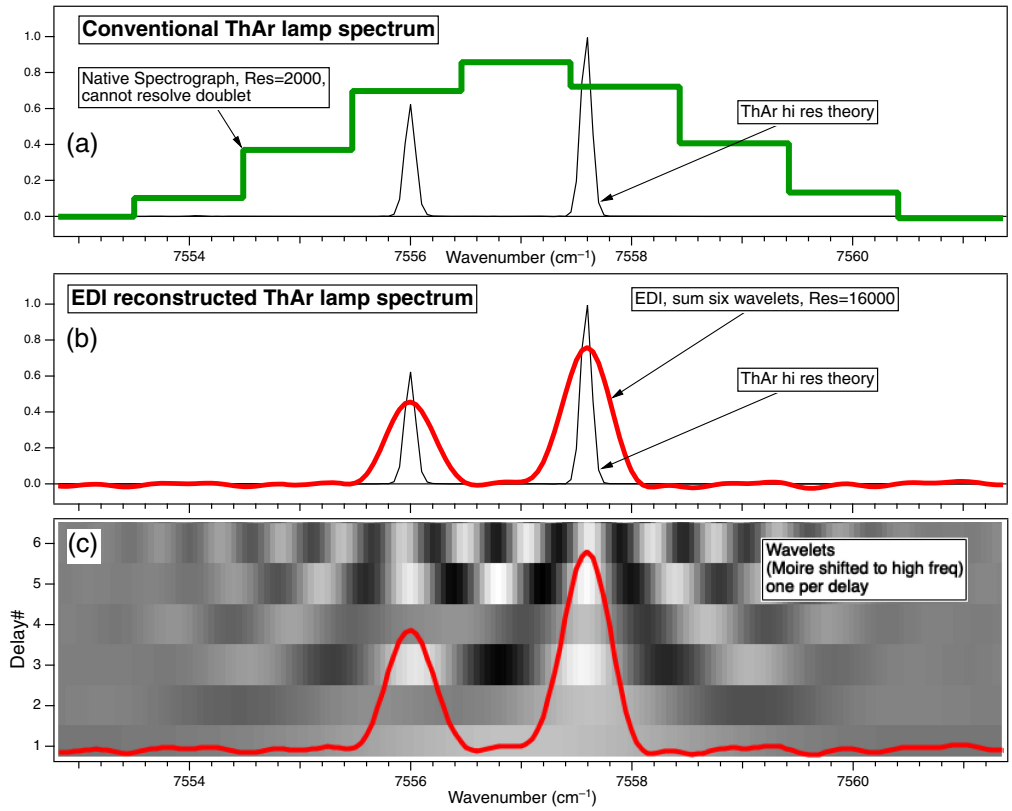

Fig. 1 Demonstration of EDI high-resolution spectroscopy at Hale Telescope,[1–3] boosting NIR TripleSpec[4] resolution ~8 times. (a) ThAr lamp measured conventionally, not resolving doublet (thin black is library spectrum). (b) EDI reconstructed spectrum (red) at $R = 16,000$ fully resolves doublet[2] and is sum of wavelets (c), one per interferometer delay.

Figure 1(a) shows that due to the TripleSpec's low resolution $R = 2000$ (green cityscape indicating pixels), it cannot resolve a ThAr lamp doublet. The spectrograph was mounted on the Cassegrain output of the telescope, [Fig. 2(left)], and thus had limitations on its weight, bulk, and suffered a changing gravity vector. Its low resolution was a cost of mounting on a mobile platform (i.e., on moving telescope mirror following stars in angle through the night). This was an example of normal tradeoffs in spectrograph design between resolution size, weight, and cost.

An interferometer in series with a dispersive spectrograph creates a hybrid instrument EDI,[1–3,5–14] which can dramatically enhance the performance of a disperser used alone. (The EDI technique has been used by other researchers to discover exoplanets[15–17] around HD102195 and HD87646, as well as confirmation of 51 Peg.[18]) We explored several EDI

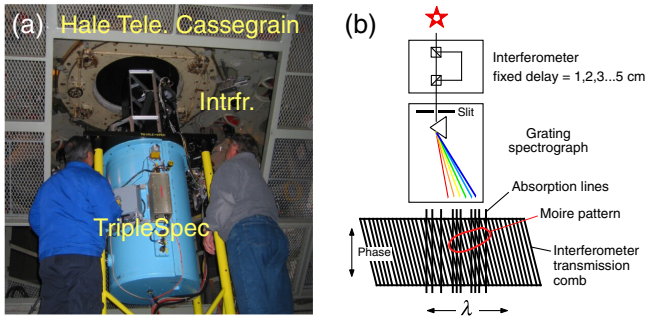

Fig. 2 (a) TripleSpec spectrograph (blue cryostat) with T-EDI interferometer (black and silver) above, attaching to Cassegrain output of 5 m Hale Telescope at Mt. Palomar, 2007–2011. (b) EDI scheme—a fixed delay interferometer crossed with disperser. Figure reproduced with permission from Ref. 2 by SPIE.

applications: Doppler radial velocimetry of M stars[1,11] and high-resolution spectroscopy.[2,3,9,10] Regarding the latter, Figs. 1(b) and 1(c) show an 8 times resolution boosting ability of EDI measuring a ThAr lamp doublet, using six of the eight interferometer delays, and summing the wavelets created by each delay when detected moiré patterns are Fourier shifted up to their original frequencies.

1.2 Prior Data Analysis Advance: Stabilization Using Pairs of Delays

More recently,[14] we explored a third EDI application: stabilization of the output spectrum against unknown and irregular drifts Δx in the disperser component of EDI (the TripleSpec). This was a new mathematical technique for processing EDI data, which we call "crossfading," after how a sound engineer gradually fades out one audio source and fades in another while maintaining nearly a constant net volume.

The crossfading (X-EDI) data analysis algorithm modifies how we mathematically combine signals of pairs of partially overlapping delays, noting that under a drift Δx, the low frequency half of the higher delay reacts oppositely in phase to higher frequency half of lower delay (Fig. 15 of Ref. 14). By strategically choosing frequency dependent weights, the net reaction to Δx of overlapping delays can be made zero or very small. This is a mathematical advance that re-analyzed older EDI data and achieved dramatic results[14] of ~1000x times less change in output peak position drift than with disperser used alone.

1.3 New Data Analysis Advance: Stabilization Using a Single Delay and the Native Spectrum

We wondered if crossfading stabilization could also work with a single delay, rather than a pair of delays, by substituting the ordinary (native) spectrum for lower delay signal, and using the single delay as higher delay. This would be an algorithm extension. The answer is yes, it works!

The purpose of present paper is to re-analyze Triplespec-EDI data using only a single delay (of eight available), to demonstrate this new method extension. Because a single delay is the most common interferometer configuration, this is a practical improvement. It is a mathematical and software advance, not a change in hardware from the classic EDI. The apparatus taking EDI data remains the same.

1.4 Concrete Motivation: Irregular Drift Seen in Our Disperser Data

Figures 3 and 4 show our concrete motivation for crossfading stabilization: a particularly egregious example of spectrograph drift, measured on the NIR TripleSpec spectrograph[4] used with the (called here) T-EDI project[1–3] on the Mt. Palomar Observatory Hale telescope. Figure 4 shows drift of features (valleys in spectrum of Fig. 3) in conventional Triplespec spectrum, over

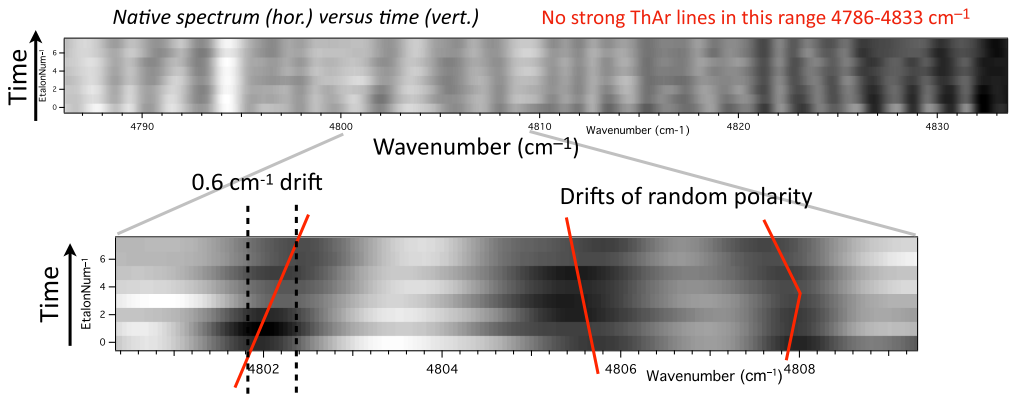

Fig. 3 Example irregular spectrograph wavelength drift measured on tripleSpec[4] used with T-EDI.[1–3] Each row is HD219134 conventional spectrum at a different time. (Quasiperiodic lines are a telluric feature—an additive white light comb was not used). Observed drift is difficult because it is bipolar irregular in magnitude (~0.6 cm^{-1}), changes over a small distance scale of 2 cm^{-1}, and no strong ThAr lines are within this range 4786–escaped;4833 cm^{-1} to calibrate. Figure reproduced with permission from Ref. 2 by SPIE.

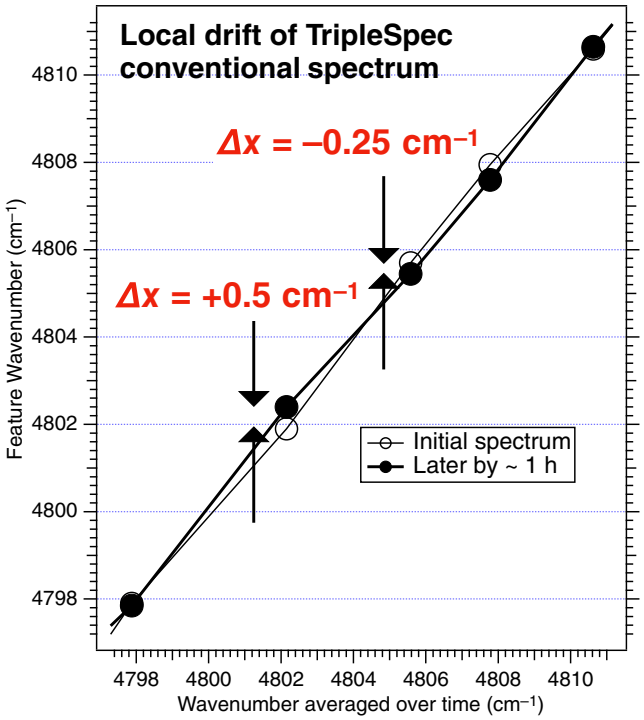

Fig. 4 Drift in conventional triplespec spectrum (Fig. 3), compared with time-averaged positions. The deviations (called Δx) are bipolar irregular, changing on scale of ~2 cm^{-1}, and of ~0.6 cm^{-1} magnitude.

~1 h, compared with time-averaged positions. The deviations are irregular (changing polarity on scale of ~2 cm^{-1}). Note that the quasiperiodic lines here are a telluric feature—an additive white light comb was not used.

This region 4786–escaped;4833 cm^{-1} is not adequately calibrated by ThAr lines (the nearest strong ones are outside at 4764 and 4849 cm^{-1}), a distance much greater than the 2 cm^{-1} scale width of irregularity. Hence, reference lines cannot sense irregularity sufficiently to correct it. The TripleSpec did not use a laser frequency comb (LFC) due to expense and its inability to resolve ($R \sim 2000$ to 3000) the LFC spikes.

2 EDI Theory and Data Analysis Equations

2.1 Multiplicative Comb Produces Heterodyning Detection

Reference 9 and Sec. 5 of Ref. 2 describe single-delay EDI theory regarding spectroscopy. In EDI, the sinusoidal comb multiplies the input spectrum $S(\nu)$, not adding to it, as with a calibrating white light comb (WLC) or laser frequency comb (LFC). Figure 2(b) shows EDI scheme is a fixed delay interferometer in series with a disperser. The interferometer transmission $T(\nu)$, also called $T_{\text{edi}}(\nu)$ in the Appendices A and B, is sinusoidal with a pitch or frequency proportional to its delay τ,

$$T_{\text{edi}}(\nu) = T(\nu) = (1/2)[1 + \cos(2\pi\tau\nu + \phi)]. \tag{1}$$

When starlight passes through it, the sine comb transmission is multiplied against the input stellar spectrum, as illustrated by the vertical black lines (stellar absorption lines) overlaying a slanted periodic comb.

$$S(\nu)T(\nu) \propto S(\nu) + S(\nu)\cos(2\pi\tau\nu + \phi). \tag{2}$$

This beam passing through disperser is blurred by the slit and focal spot and splayed out into a spectrum on detector, one exposure $B_\phi(\nu)$ for each of several interferometer phase (ϕ) step increments. The latter is implemented by mounting an interferometer cavity mirror on a PZT

transducer. The set of $B_\phi(\nu)$ are used to mathematically separate the first (native) and second (fringing) terms.

The ν is the dispersion variable wavenumbers (units cm^{-1}). The variable ν is preferred over wavelength ($\lambda = 1/\nu$), because $T(\nu)$ is periodic in ν. The Fourier variable is frequency ρ, in features per cm^{-1}, which conveniently has same units as delay τ in cm. Hence, graph horizontal axes can be labeled delay or frequency interchangeably.

2.2 Phase Stepping Math to Separate Fringing From Nonfringing

The $(1 + \cos)$ transmission behavior simultaneously creates two detectable signals: a nonfringing ordinary spectrum (multiplication by the 1) we call the "native" or B_{ord} and a fringing spectrum $\mathbf{W}$ (multiplication by the cos).

Nonfringing (native or ordinary) and fringing components are separable during analysis because data is taken in a phase-stepped manner in at least three exposures while incrementing delay by a subwavelength amount $\delta\tau$. This produces a phase shift ($\delta\phi = \nu\delta\tau = \delta\tau/\lambda$) in cycles. For illustrative purposes, for four exposures every 90 deg yields algebraically simple equations

$$B_{\mathrm{ord}}(\nu) = \frac{1}{4}(B_0 + B_{180} + B_{90} + B_{270}). \tag{3}$$

$$\mathbf{W}(\nu) = \frac{1}{4}[(B_0 - B_{180}) + i(B_{90} - B_{270})]. \tag{4}$$

In reality, the phase shift amount varies across the band as ($\delta\phi = \nu\delta\tau$); our algorithm in Sec. 5 of Ref. 2 accommodates such irregular phase step values.

2.3 Moiré Is Product of a Multiplying Sine Comb

Regarding the fringing term $\mathbf{W}(\nu)$, the multiplication of a spectrum $S(\nu)$ times a sinusoid creates moiré patterns, which can appear as bead-like patterns. The moiré are high frequency spectral information shifted down to lower frequency optically in a process called heterodyning (Fig. 5). The $\mathbf{W}(\nu)$ is complex to represent fringes having phase and magnitude.

Because moiré are broad, they are insensitive to distortions in spectrograph point spread function (PSF) and the Nyquist frequency limit (set by half the pixel density). This allows EDI to detect high frequencies otherwise unresolvable by the spectrograph alone. Mathematics reverses the heterodyning and shifts moiré up to restore its original frequency. This creates wavelet features in the output spectrum, seen in instrument response [Fig. 6(a)]. Figure 6(b) shows EDI response in frequency (ρ). Heterodyning shifts the EDI sensitivity peak from the origin to τ.

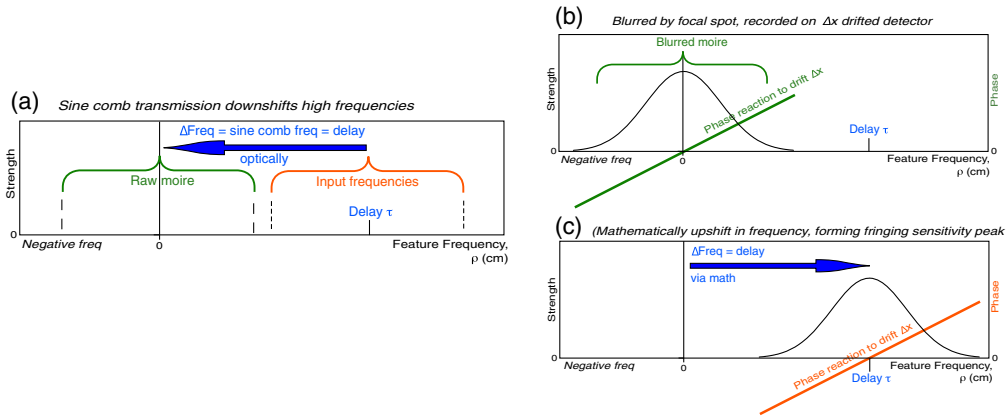

Fig. 5 Explanation in frequency (ρ) space of why the fringing phase reaction line occurs at delay, $\rho = \tau$. (a) High frequencies are heterodyned (downshifted by $\Delta\rho = \tau$) to form moiré near zero by multiplication of sine comb. (b) Moiré are blurred. Translation on detector by drift Δx rotates frequencies by $e^{i2\pi\rho\Delta x}$. (c) During analysis moiré are upshifted by τ to original high frequencies. This also shifts fringing phase reaction line to $e^{i2\pi(\rho-\tau)\Delta x}$ (red line), flipping polarity at $\rho = \tau$.

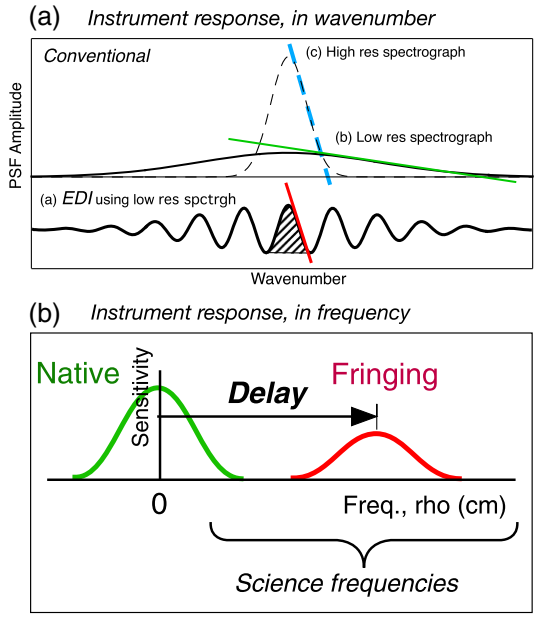

Fig. 6 (a) Instrument response of EDI in wavenumbers (cm^{-1}). (b) Instrument response in frequency (ρ), units features per cm^{-1} or cm. Heterodyning shifts fringing sensitivity peak (red) from origin up to frequency set by delay. Wavelet (a) is Fourier paired with fringing peak (red). Low resolution PSF (b) paired with native peak (green). Figures reproduced with permission from Ref. 2 by SPIE.

2.4 Why Phase Reaction Line Flips Polarity

Figure 5 explains why the fringing phase reaction line (red) changes polarity at the delay, $\rho = \tau$. (a) High frequencies are heterodyned down to form moiré near zero frequency. In panel (b), moiré are blurred by spectrograph (frequencies attenuated by Gaussian-like peak). Translation on detector by drift Δx rotates frequencies by $e^{i2\pi\rho\Delta x}$. The exponential argument is phase reaction line $\phi = \rho\Delta x$, which flips polarity for negative frequencies. (c) Moiré are mathematically upshifted by τ and fringing phase reaction line (red) shifted to $e^{i2\pi(\rho-\tau)\Delta x}$, so it flips polarity at $\rho = \tau$. (Having zero phase reaction in ρ-space means moiré in ν-space are horizontal and thus insensitive to Δx.)

2.5 Data Analysis After Phase Stepping

Equations on phase stepped data analysis are from Ref. 2, Secs. 6.5, 7.3, and 7.4. Complex $\mathbf{W}(\nu)$, representing moiré fringes having phase and magnitude, is first rebinned to finer pixels (we use 0.05 cm^{-1}).

2.5.1 *Untwisting effect of glass dispersion*

The interferometer delay is a slow function of ν due to refractive index of glass etalon. This creates a phase twist $\theta_{\text{glass}}(\nu)$. Data $\mathbf{W}(\nu)$ are untwisted via

$$\mathbf{W}(\nu)_{\text{untwist}} = \mathbf{W}(\nu)e^{-i2\pi\theta_{\text{glass}}(\nu)} \tag{5}$$

to remove effect of glass dispersion. Example $\theta_{\text{glass}}(\nu)$ data is in Sec. 9.

2.5.2 *Reversal of heterodyning*

Heterodyning is easily reversed by complex multiplication in ν-space,

$$\mathbf{W}'(\nu) = e^{-i2\pi\nu\tau}\mathbf{W}(\nu)_{\text{untwist}}, \tag{6}$$

rather than shifting in ρ-space, because multiplication presents no issues with continuous values of τ. (We found shifting in ρ-space led to quarter cycle sized phase errors due to discrete nature of Fast Fourier Transform [FFT]). A negative value of τ in exponent is because of our (arbitrary)

convention to have fringe comb spike be a positive frequency. Then, Eq. (6) shifts this spike to left to zero frequency (representing the stellar continuum) while also moving moiré from near zero to increasingly negative frequencies. We take the real part

$$\Omega(\nu) = \mathbf{W}'^{*} + \mathbf{W}' = 2\Re\mathbf{W}'(\nu), \tag{7}$$

to form a scalar spectrum, having wavelets [similar to Fig. 6(a)] for each line feature in the input spectrum.

2.5.3 *Combining weighted signal components*

Wavelets summed form a provisional spectral reconstructed (SR) output SR_{raw}

$$\text{SR}_{\text{raw}}(\nu) = B_{\text{ord}}(\nu) + \Omega(\nu). \tag{8}$$

when the purpose is high resolution spectroscopy because B_{ord} contributes low-frequency information insufficiently measured in by fringing (Ω). The above is classic-EDI result (i.e., not using crossfading).

For crossfading we apply ρ-dependent weights (filtering) $k_n(\rho)$ to the Fourier Transform (FT) of $B_{\text{ord}}(\nu)$, represented by lower case $b_{\text{ord}}(\rho)$, and similarly for FT of wavelets $\Omega(\nu)$, called $w(\rho)$.

$$\text{sr}_{\text{Xraw}}(\rho) = k_0(\rho)b_{\text{ord}}(\rho) + k_1(\rho)w(\rho). \tag{9}$$

Details of how weights $k_n(\rho)$ are chosen is discussed later. Only the ratio between them matters because subsequent equalization will adjust their common mode value. For example, we use $k_1 = 1$ for simplicity, and only choose values for k_0.

2.5.4 *Applying equalization to reduce ringing*

The sr_{Xraw} is stabilized, but because its modulation transfer function (MTF) is most likely non-Gaussian, it may have ringing. This is solved by multiplication by a purely real equalization $\text{eq}(\rho)$

$$\text{sr}_{\text{Xedi}}(\rho) = \text{sr}_{\text{Xraw}}(\rho)\text{eq}(\rho), \tag{10}$$

$$\text{mtf}(\rho) = \text{sr}_{\text{Xraw}}(\rho)/s_{\text{thry}}(\rho), \tag{11}$$

$$\text{eq}(\rho) = \text{gaussian}(\rho)/\text{mtf}(\rho). \tag{12}$$

The MTF is the frequency response of EDI, comparing measured sr_{Xraw} with theoretical shape sr_{thry} at a strong ThAr spectral line. This computes equalization $\text{eq}(\rho)$, which is limited to a ceiling so that in the wings where MTF is small the EQ does not excessively magnify noise. We zero out $\text{eq}(\rho)$ in regions, in which the $\text{sr}_{\text{Xraw}}(\rho)$ is expected to be zero. The $\text{sr}_{\text{Xedi}}(\rho)$ is inverse FT'd to form the output spectrum $\text{SR}_{\text{Xedi}}(\nu)$.

2.6 Doppler: Stellar Minus Reference

For Doppler velocities using a simplified EDI analysis (Sec. 7.2–8 of Ref. 8), we can work directly with the moiré data, not needing to reverse the heterodyning to form a formal output spectrum (although that is an option to use with software that is expecting that). (A more formal and comprehensive T-EDI Doppler analysis that includes effects of telluric artifacts, large barycenter velocity shifts and detector idiosyncrasies is Ref. 1.)

To be immune to slight drifts in delay, we subtract the reference lamp ThAr moiré fringe phase θ_{Ref} from the stellar fringe phase θ_{Stellar}, because both will be similarly affected by a slight delay change.

$$V_D = \text{VPF} * [\theta_{\text{Stellar}} - \theta_{\text{Ref}} + \text{const}], \tag{13}$$

$$\text{VPF} = c\lambda/\tau = c/(\nu\tau), \tag{14}$$

is the velocity per fringe (VPF) proportionality and c is velocity of light. (VPF for 1.1 cm delay at $19,500\ \text{cm}^{-1}$ in Ref. 9 is 14 km/s per fringe; VPF for T-EDI in Ref. 1 at $4800\ \text{cm}^{-1}$ for 4.6 cm

E8 delay is 13.5 km/s, for 0.66 cm E3 is 95 km/s.) Because the constant in Eq. (13) is initially unknown, V_D measures velocity changes relative to an initial datum or other standard.

3 Classic (Noncrossfading) EDI

Figure 7 shows in frequency space how a classic (noncrossfading) EDI, which used a single delay and ignored the native spectrum, had two desirable behaviors: high Doppler velocity sensitivity and some stability against disperser drifts Δx. These qualities enabled an inexpensive compact apparatus to have m/s scale precision[6–8] while not employing conventional mitigations to reduce spectrograph drifts. The high Doppler sensitivity comes from heterodyning. Stability comes from the phase reaction line (red line) crossing zero at $\rho = \tau$. This is the most stable frequency, because feature and comb have same frequency, producing a horizontal moiré (for slanted comb graphics as in Fig. 7). For a horizontal moiré there is zero phase reaction to Δx.

3.1 Motivation to Implement Crossfading for an Existing EDI

A problem with the classic version of EDI is that zero reaction only occurs at a single frequency, not a range. An arbitrary spectrum has an arbitrary distribution over a frequency range. An ideal spectrograph should have zero phase shift for all frequencies.

3.2 Wavelet Frequency Halves Behave Oppositely

Figure 8 illustrates wavelet behavior when it is filtered to suppress high frequencies—only containing low. It moves in opposition to the Δx drifted native spectrum. This provides the means for canceling out the net reaction to Δx, if native and low-frequency signals are combined with strategically chosen frequency dependent weights. Opposition provides large negative feedback (iterating in a conceptual control loop) to converge rapidly to a stable spectrum and revealing Δx when it is initially unknown.

In an earlier paper[14] using pairs of delays, opposing reactions were two overlapping delays. In this paper, the opposing reactions will be the lower half of a single delay and the native peak.

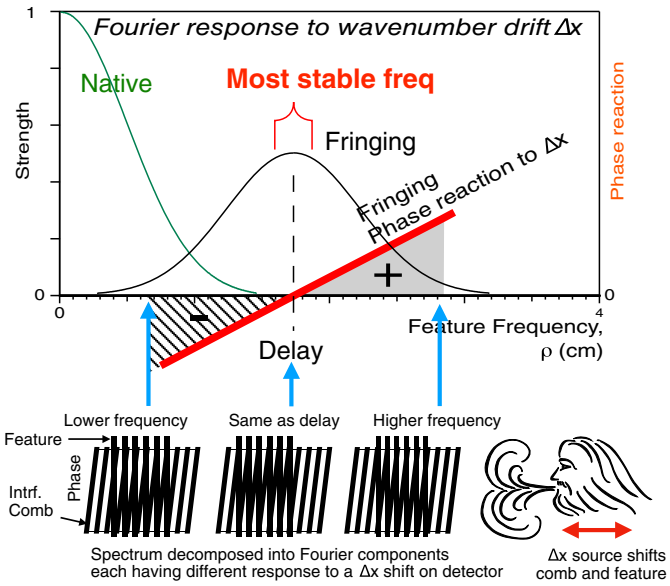

Fig. 7 (Top) frequency-space illustration of classic EDI, having single delay τ but ignoring native spectrum. Fringing phase reaction line (red line) crosses zero at peak center $\rho = \tau$, the most stable frequency, because its moiré is flat and immune to Δx. However, arbitrary spectra contain a range of frequencies. Crossfading algorithm is stable over a range. (Bottom) Moirés having different slants at different ρ. Translation of moiré (wind icon) by Δx evokes different polarity reactions versus ρ.

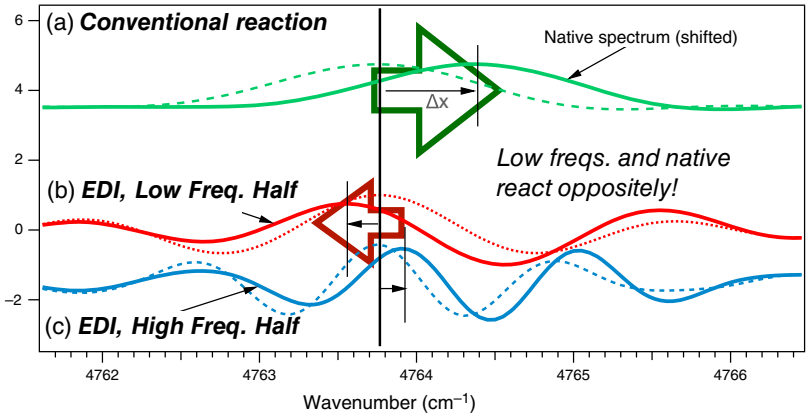

Fig. 8 Illustration in ν of low and high frequencies halves of EDI wavelet reacting oppositely to Δx (dashed/dotted to bold curves). (a) Native (green) has direct reaction $\Delta\nu = \Delta x$. (b), (c) EDI frequencies split into (b) low (red) and (c) high (blue) wavelets (at $\rho = \tau$) react oppositely, confirming polarity flipping of reaction line in ρ-space (Fig. 5). Significantly, (b) low-frequency wavelet reacts oppositely to Δx. This is means zero net reaction to Δx if native and low frequencies are combined strategically.

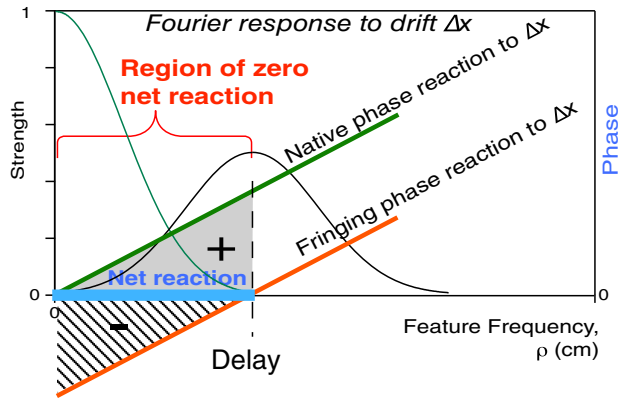

Fig. 9 Crossfading scheme using a single fringing peak overlapping native peak. Under Δx the two signal types have opposite phase reactions for $\rho \leq \tau$. Combining using ρ-dependent weightings, native (green) and fringing (red) reactions cancel (blue thick line having zero phase versus ρ).

4 Crossfading Method

4.1 Modern Crossfading Method Using Single-Delay

Figure 9 illustrates the improved (single-delay) crossfading scheme, where instead of two overlapping delays, the native sensitivity peak overlaps a single fringing peak. Between frequencies $0 < \rho < \tau$, the native reaction phase line (green) opposes the fringing reaction line (red). Weightings (shown later) cancel the net phase for that range (blue line). Frequencies above center of fringing peak, $\rho > \tau$, are ignored during early iterations, but can be included during last (to produce ~2x resolution boost).

The technique has practical advantage over paired-delay crossfading because single-delay interferometers are the default format and easier to construct than multiple delay interferometers. Second, the optimal condition where opposing signals to stem from same Δx for most accurate cancellation, is automatically satisfied, because native and fringing signal components are obtained from same data.

4.2 Simple Crossfading Model with Triangular Lineshape

Figure 10 shows a simple mathematical model to explain crossfading, using a triangular shape for the MTF. Imagine that filtering has reshaped MTF from its original shape into a symmetric

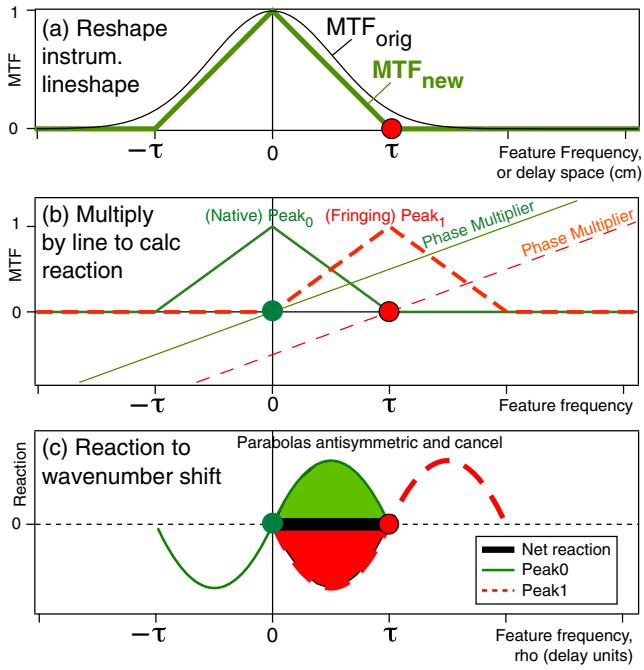

Fig. 10 Simple mathematical model to explain crossfading, using triangular shape for MTF. Imagine ρ-dependent weights (filtering) reshape MTF into a symmetric triangle having full width twice the delay (τ), deleting native spectrum signal above $\rho > \tau$. Fringing component of MTF is copy of native at higher frequency. Fourier mathematics shows drift Δx in ν-space modifies MTF in ρ-space by multiplication by line versus ρ, indicated on (b) as phase multiplier. Hence, there are two linear functions in ρ, multiplying each other to create quadratic dependence on ρ, depicted by solid green parabola between 0 and τ. This parabola is phase reaction of native component to Δx. A corresponding solid red parabola for fringing has opposite polarity. These can cancel, forming zero net phase reaction (bold black line between 0 and τ). This implies net MTF for this frequency range is robust to Δx.

triangle having full width exactly twice τ, suppressing the native spectrum signal above $\rho > \tau$. (The fringing component of MTF is a copy of native translated by τ.)

Fourier transform mathematics shows that Δx in ν-space modifies MTF in ρ-space by multiplication by ρ, indicated in (b) as phase multiplier. (This comes from the derivative of $e^{i2\pi\rho\nu}$ with respect to ν, which brings down a copy of the $i\rho$ term from the exponent.) From Sec. 9.4 of Ref. 2, the phase reaction to Δx is

$$\text{Reaction}(\rho) \propto (\rho - \tau_n)\text{psf}(\rho - \tau_n)\Delta x. \tag{15}$$

For native MTF, $\tau_0 = 0$ and we have

$$\text{Reaction}(\rho) \propto \rho\text{psf}(\rho)\Delta x. \tag{16}$$

For the fringing MTF, $\tau_n = \tau_1$ and we have

$$\text{Reaction}(\rho) \propto (\rho - \tau_1)\text{psf}(\rho - \tau_1)\Delta x. \tag{17}$$

The net reaction is

$$\text{NetReaction}(\rho) \propto [\rho\text{psf}(\rho) + (\rho - \tau_1)\text{psf}(\rho - \tau_1)]\Delta x = 0, \tag{18}$$

where we set it to zero to solve for the cancelation condition. The Δx factor divides out. Hence, weightings that produce cancelation for small Δx, it will work for both polarities and a range of values. Hence, for the triangle, two linear functions in ρ multiplying each creates quadratic on ρ (green parabola between 0 and τ). This is the native phase reaction to Δx. The corresponding fringing red parabola has opposite polarity. These can cancel, forming a zero net phase reaction (bold black line between 0 and τ). The net MTF for this frequency region is robust to Δx.

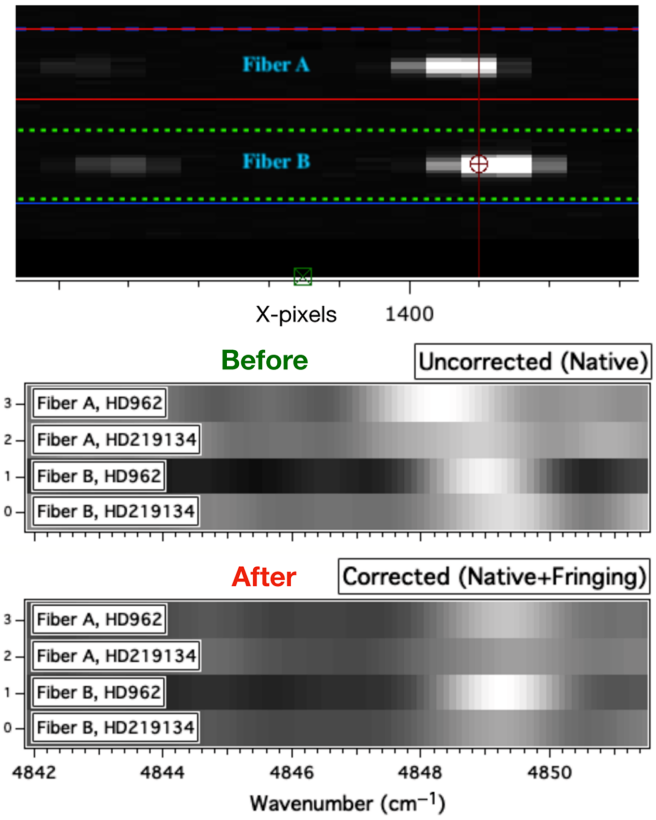

Fig. 11 Demonstration of single-pass crossfading correction on TripleSpec spectrograph data.[2] (Top) detector image of ThAr lamp alone—geometry of echelle optics causes ThAr line to displace ~1 pixel, (~0.6 cm^{-1}) between fibers A and B. (Middle, Bottom) "Before" and "After" versions of four stacks of spectrum lineouts versus wavenumber, from HD962 and HD219134 with ThAr. Four instances of Δx are sum of fiber offsets and natural drift (~1 h). (Bottom) "After" panel shows data processed with crossfading successfully corrects drifts—note vertical alignment of features.

5 Results

5.1 Demonstration of Crossfading on Data From Different Nights

Figure 11(top) shows a small section of echelle spectrograph image measured[2] with TripleSpec[4] September 2010. This is starlight with added ThAr lamp, from stars HD962 and HD219134, each in two optical fibers A & B. Due to echelle optical geometry, the positions for same ThAr line are displaced by ~1 pixel, creating ~0.6 cm^{-1} offset between fibers. Figure 11 (middle) shows drift over ~1 h as targets changed between stars—creating four different naturally generated Δx in four rows of "Before" panel. Figure 11 (bottom) the "After" panel shows crossfading successfully correcting the four different amounts of the insult Δx. (Note final vertical alignment). A 4764 cm^{-1} ThAr line (off graph) provides absolute reference for interferometer phase.

5.2 Simulation of Crossfading on Very Irregular Drift

Figure 12 shows demonstration of crossfading correcting a bipolar irregular drift with a single pass on a synthetically distorted version of a measured spectrum, similar to measured TripleSpec[4] data (Fig. 3). Artificial distortion grew in an "M" shape between 4826 and 4846 cm^{-1}, with amount 0 to $+0.6$ cm^{-1}, to -0.6, $+0.6$, returning to 0 [Fig. 12(a)]. A bipolar distortion is the most challenging type to correct without nearby spectral lamp calibration lines. Output of single pass of crossfading; parallelism of features indicates success [Fig. 12(b)].

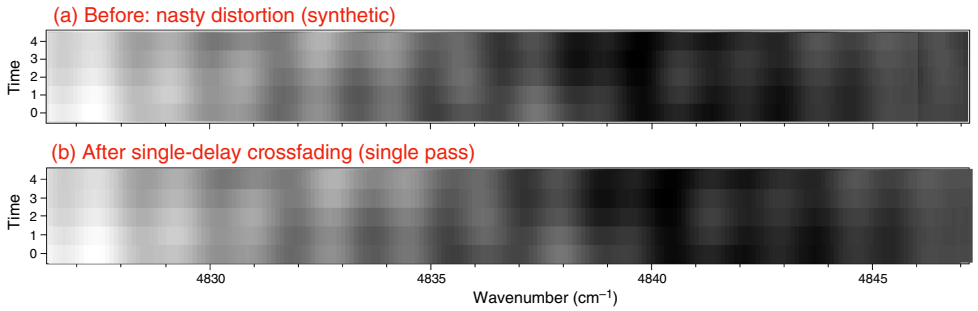

Fig. 12 Demonstration of single-pass crossfading correcting bipolar irregular drift on simulated data similar to Fig. 3. (a) Input was TripleSpec[4] data (Fig. 3) artificially distorted, each row a different amount, in "M" shape between 4826 and 4846 cm^{-1}, shifting -0.6 to $+0.6$ cm^{-1}. (b) Result after single-pass crossfading—parallelism of features indicates success. Note that the quasiperiodic lines are a telluric feature, not an additive white light comb.

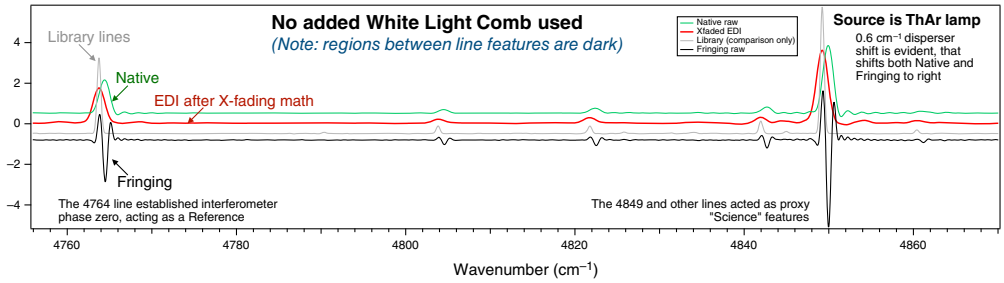

Fig. 13 Evidence that crossfading EDI does not use an additive white light comb, because it would appear between ThAr line features, and we observe darkness. This is because our sine comb "ruler" is multiplicative, not additive. The 4764 cm^{-1} ThAr line and its library (gray) position established interferometer phase zero. Other library lines not used for computations. Large line at 4849 cm^{-1} and smaller lines elsewhere are proxy "science" features demonstrating crossfading correction (red) compared with drifted native (green). Curves vertically offset.

5.3 Evidence That Additive White Light Comb Not Used

Figure 13 shows that crossfading EDI does not use an additive white light comb, because darkness appears between ThAr lines. These regions are dark because our sine comb is multiplicative, not additive, and zero times a sine is zero. Curves are vertically offset for clarity. The 4764 cm^{-1} ThAr line and its library (gray) position established interferometer phase zero. Other library lines were not used for computations and are guide for eye to other features. Large line at 4849 cm^{-1} and smaller lines elsewhere are proxy "science" features demonstrating crossfading correction.

6 Real-World Implementation of Crossfading

6.1 Small Computational Window Minimizes Parameters to Solve

It is advantageous to use a small computational bandwidth window of 200 points (10 cm^{-1}), just 7 times native PSF full width at half max (FWHM), and not the full bandwidth which is $\sim$26,000 points. This dramatically reduces the number of weights to compute to seven in our case. The FT of 0.05 cm^{-1} bins has Nyquist range of -10 to $+10$ cm. Dividing this into 200 produces 0.1 cm spacing on the FT. Then, the 0.66 cm delay E3 needs seven weights from 0 to 0.6 cm (Table 1).

6.1.1 *Application of weights to a wider bandwidth*

To apply weights to wider bandwidth data, such as 114 cm^{-1} region of Fig. 13, having 11 times the computational bandwidth (Sec. 6.1), we interpolate weight functions to the smaller units that appear when taking FT of larger bandwidths. (Because native PSF may slowly change with ν, the crossfading weight choice could be recomputed at several locations.)

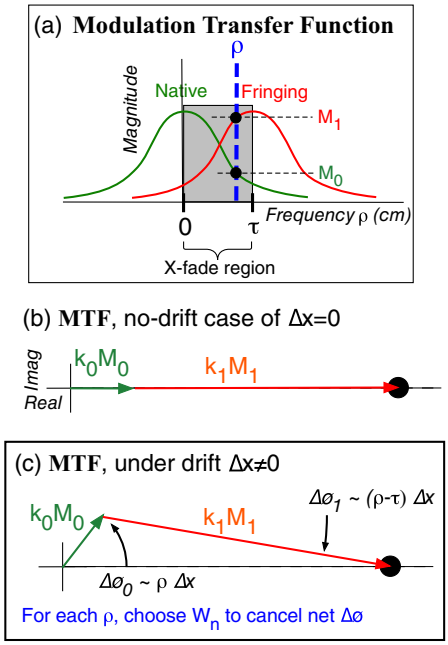

Fig. 14 Vector construction for choosing ρ-dependent weights to nearly cancel net phase reaction to Δx. (a) MTF is ρ-space Fourier transform of the instrument lineshape in ν. (b) Undrifted case ($\Delta x = 0$). (c) Drifted case ($\Delta x \neq 0$). Ratio of weights $k_0(\rho)$ and $k_1(\rho)$ are chosen to modify MTF magnitudes $M_0(\rho)$ and $M_1(\rho)$ to produce cancellation in panels (b) and (c).

6.2 Choice of Weights to Satisfy Vector Cancelation

Figure 14 shows our vector construction scheme for choosing ρ-dependent weights. The ratio of weights $k_0(\rho)$ and $k_1(\rho)$ modifying MTF magnitudes $M_0(\rho)$ and $M_1(\rho)$ (vector length in [b][c]) are chosen for each ρ. Because only the ratio matters, we hold $k_1 = 1$ for simplicity.

For a given ρ, the MTF has a complex value, magnitude and phase, represented by vectors in panels (b) and (c). We desire vector cancelation of the imaginary component, which is perpendicular to main vector direction, because this affects phase and thus position of peaks in ν-space.

Theory shows that under a Δx, the MTF rotates by angle $\Delta\phi \propto \rho\Delta x$, for native component, while fringing component rotates by $(\rho - \tau)\Delta x$. Thus, for low frequencies $\rho < \tau$, fringing rotates opposite as native. Then, weight choice yields cancelation (using small angle approximation to the sine function). The magnitude may also change slightly but canceling phase is more important, because that controls peak position.

Figure 15 shows our software's geometric construction screen to find optimal weight ratios, here, for $\rho = 0.4$ cm case. Successful weight choice achieves minimal vector change for three values $\Delta x = -0.5$, 0 and $+0.5$ cm^{-1}, shown for sum vector (blue open diamonds), native (green circles), and fringing (red squares). The vectors are complex FT of a ThAr line, for ρ from 0 to 0.7 every 0.1 cm. For $\rho = 0.4$ of this figure, we choose native weight of 2.23 and fringing of 1. Note the colinearity of the three open blue diamonds, indicating success. Results for all ρ are in Table 1.

Figure 16 compares using, and not using, Table 1 weights on displacement reactions in the crossfading example—etalon E3 (0.66 cm) (red curve) and native spectrum (green curve). Multiplying weights against raw data (open circles and squares) forms curve with solid markers. This makes native curve (bold green) more ideally antisymmetric to fringing curve (bold red), improving cancelation.

This figure shows displacement reactions of 4764 cm^{-1} ThAr peak, for both E3 and native, computed using $\Delta x = 0.5$ cm^{-1} (similar to Fig. 27 of Ref. 14 showing displacement reactions for many different delays). The E3, having a delay of 0.66 cm, in which the curve crosses 0, is chosen for our demonstration rather than E2 or E4 (0.34 and 0.96 cm), because its negative going curve portion nicely aligns with positive going portion of native curve. The "S" shape is due to phase reaction line (red line in Fig. 7), which crosses zero at delay 0.66, times the lineshape.

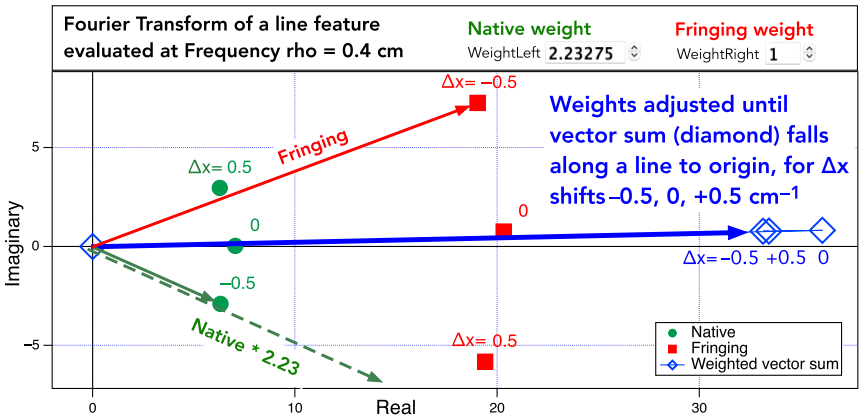

Fig. 15 Geometric construction screen in our software, used to find optimal weight ratios, here for $\rho = 0.4$, so that sum vector (blue open diamonds) of native (green circles) and fringing (red squares) vectors changes minimally for $\Delta x = -0.5$, 0 and $+0.5$ cm^{-1}. This indicates that sum phase is independent of Δx, i.e., stable. Vectors are complex values of Fourier transform of a ThAr line, for native (green), and E3 delay of fringing (red). Results for all ρ are in Table 1.

Table 1 Relative weights for each frequency ρ (0 to 0.7 by 0.1 cm), which satisfies vector cancelation (Fig. 15), for native spectrum (middle) and fringing delay E3 (right). Only ratio between middle and right values matters, because later equalization multiplies both.

Frequency (cm)	Weight of native	Weight of delay E3
0	1	0
0.1	0.915	1
0.2	1.386	1
0.3	1.792	1
0.4	2.233	1
0.5	2.700	1
0.6	4.370	1
0.7	0	0

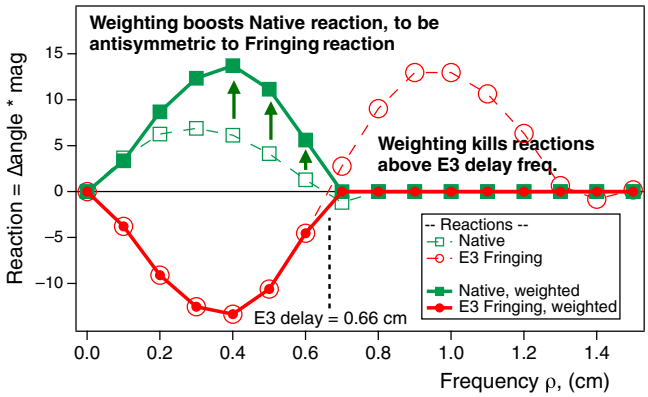

Fig. 16 Effect of multiplying chosen ρ-dependent weights of Table 1 against raw data (open circles and squares) is to form curves with solid markers. This makes reaction of native curve (bold green) antisymmetric to fringing curve (bold red), so they cancel. Frequencies above E3 delay ($\rho > 0.66$ cm) are deleted, because they have same polarity and do not cancel. These are displacement reactions of the "calibration" ThAr peak at 4764 cm^{-1}, for etalon E3 (0.66 cm) (red curve) and native (green curve), using $\Delta x = 0.5$ cm^{-1}.

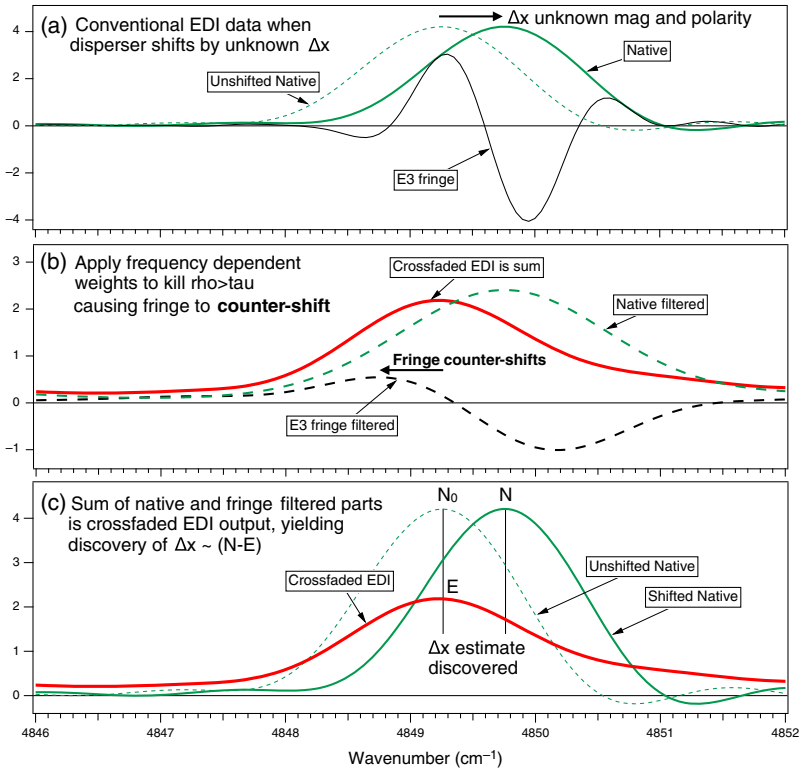

Fig. 17 Simulation of single pass crossfading on 4849 cm^{-1} ThAr line under drift $\Delta x = 0.5$ cm^{-1}. (a) Shifted native (solid green) and E3 fringing (black). Unshifted native is dotted green and is unknown by algorithm. (b) Frequency dependent weight $k_0(\rho)$ (i.e., filtering) applied to native (dashed green) and $k_1(\rho)$ to fringing (black dashes). This slightly broadens native peak (high frequencies suppressed) and shifts fringing peak opposite direction of Δx. (b), (c) The sum is crossfaded EDI output (bold red). (c) We compare peak position (E) of crossfaded EDI output to position N of native to form (N-E), which estimates Δx. Using (N-E) as negative feedback, we shift raw data by $-\Delta x$ and repeat process iteratively from panel (a). Algorithm does not need initial value of Δx; after converging it outputs Δx.

6.3 Single Pass Demonstration with Filtered Curves Shown

Figure 17 shows a simulation of single pass crossfading on measured 4849 cm^{-1} ThAr line (our "science" line) under imposed $\Delta x = 0.5$ cm^{-1}. Shifted version of native (solid green) and shifted fringing (black) of E3 [Fig. 17(a)]. Unshifted native (dotted green) is not known by algorithm. In panel (b), ρ-dependent weight $k_0(\rho)$ (filtering) is applied to native (dashed green) and $k_1(\rho)$ fringing (black dashes). These slightly broaden native peak (since some high frequencies deleted) and shift fringing peak opposite to Δx. These two signals summed form the crossfaded EDI output (bold red) in panels (b) and (c). In panel (c), we compare peak position (E) of crossfaded EDI output to peak position N of native to form (N-E), which estimates Δx. (Note that bold red curve is close to unshifted native (dashed green, N_0) indicating high estimate quality.)

We use (N-E) as negative feedback to shift raw data by $-\Delta x$ and repeat process iteratively from panel (a). The algorithm does not need to know the value or polarity of Δx, because Δx divides out of small-signal reaction Eq. (18). The 4764 cm^{-1} ThAr line off graph calibrates interferometer phase. After converging, the crossfading algorithm yields Δx.

6.4 Optional 2x Resolution Boost

Figure 18 shows that after discovering Δx and correcting raw data by $-\Delta x$, an optional final step is to recompute EDI output with equalization (for sum of native and raw fringing) that produces $\sim 2x$ resolution boost. This now uses all the fringing frequencies—not suppressing the high. Single delay resolution boosting was performed on the Lick Hamilton echelle spectrograph in 2002.[9]

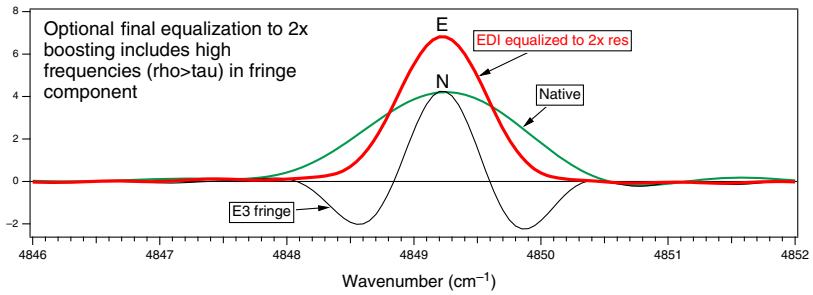

Fig. 18 After crossfading discovers Δx and corrects raw data by $-\Delta x$, an optional final step is to recompute EDI output with equalization (filtering sum of native and raw fringing signal to reduce ringing) that produces an ~2x resolution boost. (Example single delay resolution boosting was performed on the Lick Hamilton echelle spectrograph in 2002.[9])

6.5 Transfer Function for Single-Delay

Figure 19 shows stability transfer function (output offset $\Delta\nu$ versus input offset Δx), for a single pass of single-delay crossfading. In earlier publications,[2] we assumed drift error $\Delta\nu$ would depend on insult Δx linearly with slope we called translational reaction coefficient (TRC), $\text{TRC} \equiv (\Delta\nu/\Delta x)$, and we defined a stability gain G its reciprocal $(\Delta x/\Delta\nu)$. So that drift error is

$$\Delta\nu = \text{TRC} * \Delta x = \Delta x/G. \tag{19}$$

Note, for a conventional spectrograph TRC $= 1$ and $G = 1$. Figure 19 shows linearity occurs, provided Δx is smaller than about half FWHM of native spectrograph PSF, $\sim \pm 0.75$ cm^{-1}, (black diamonds). We used our data processing software on 4849 cm^{-1} ThAr data, with artificial displacements Δx. (The optional final 2x resolution boosting not applied.) We observe a slope TRC of ~0.05 (dashed green line) so the (reciprocal) stability gain G is ~20x. This TRC is much smaller than a conventional spectrograph used without EDI.

(The TRC for multiple delays can be even smaller, such as 0.001 seen for six delays in Fig. 30 of Ref. 14. This is because TRC tends to scale inversely proportional to average delay, and for multiple delays, the concatenated delay region is larger.)

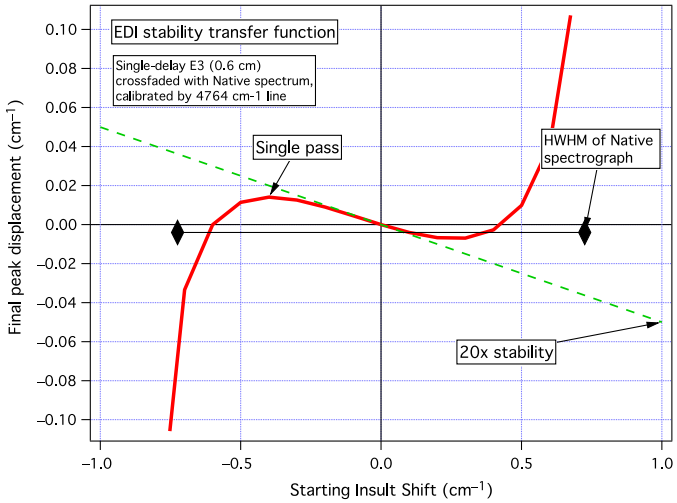

Fig. 19 Stability transfer function (output offset $\Delta\nu$ versus input offset Δx), for single pass of single-delay crossfading. We used measured ThAr data, but with artificial Δx. The 4849 cm^{-1} ThAr line (our "science" line) used weighting coefficients chosen from reactions at 4764 cm^{-1} line (our "calibration" line). This shows linear regime where crossfading works is $\Delta x < \sim \pm 0.75$ cm^{-1} a distance of one FWHM of native PSF (black diamonds). Here, the output $\Delta\nu$ is linear to input Δx with slope (TRC $= \Delta\nu/\Delta x$) of ~0.05 (dashed green line). Hence, the stability gain (reciprocal of TRC or $\Delta x/\Delta\nu$) is ~20x. Iterative passes of crossfading can further improve stability by several orders of magnitude.

7 Iterative Application of Crossfading

We have performed iterative application of crossfading, using ThAr line at 4849 cm^{-1} as "science" line and 4764 cm^{-1} line as "calibration" to establish interferometer phase. Phase opposition (Figs. 8 and 9) provides large negative feedback during iterations (in conceptual control loop) converging rapidly to a stable output spectrum and yielding Δx.

During first pass the distance "(N-E)" between native peak (N) and EDI result (E) is found as 0.53 cm^{-1} [31 km/s Doppler]. The (N-E) is negative feedback signal. For second iteration, we translate raw data by -0.53 cm^{-1} and re-apply crossfading, reducing (N-E) to 0.0086 cm^{-1}. Subsequent iterations reduce (N-E) to -4×10^{-4}, 2×10^{-5}, -1.4×10^{-6}, -2.6×10^{-7}, and 4×10^{-7} cm^{-1} [2.5 cm/s Doppler] on the 7th iteration. Hence, relative to 0.5 cm^{-1} initial Δx, we achieve ~1300x stability in three iterations, and $\sim 10^6$ stability gain in 6 iterations.

The initial Δx was relatively large, pixel-sized, because this occurs in our TripleSpec measurements. The size is also useful for naked eye discernibility in figures. However, many astronomical spectrograph have much smaller Δx because of conventional mitigations. We have not yet fully explored what sets convergence floor for extremely small (~cm/s) scale, so this work is preliminary.

7.1 Results of 2x Resolution Boost on Iteration

After many iterations E & N are trustworthy, so we can optionally include all frequencies of fringing signal (not suppressing $\rho > \tau$), then re-do equalization to a higher resolution about twice its original (Fig. 18). In this case, (N-E) increased to -0.0018 cm^{-1}, which is ~300 times stability rather than a million. This mild worsening is due to the high frequency portion, which does not face an opposing signal in a feedback loop.

8 Summarizing Notional Steps in Crossfading Process

Figure 20 shows notional steps of crossfading for a single delay and native spectrograph (green), displayed in Fourier space versus frequency ρ in cm (i.e., MTF). (a) Lower and

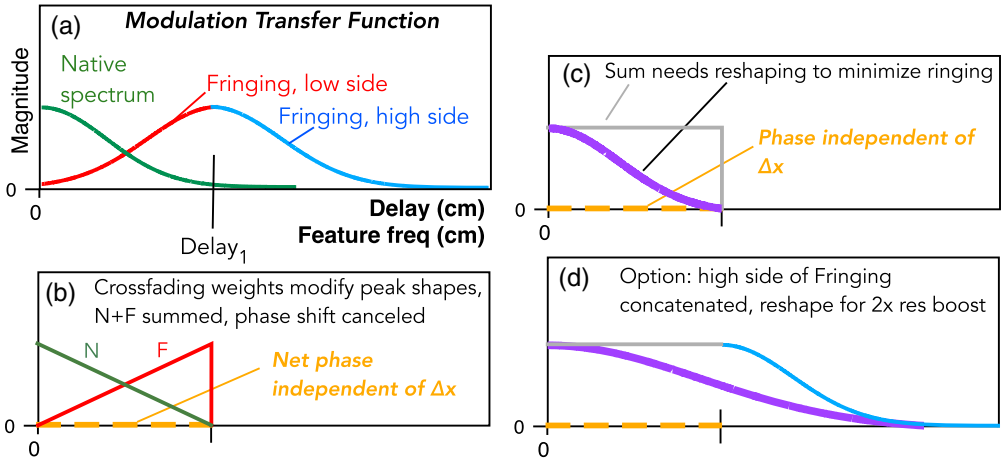

Fig. 20 Notional steps in crossfading algorithm, in plots versus frequency ρ in centimeters. (a) Fringing MTF (red/blue peak) has same shape as native (green peak at origin) but is centered at $Delay_1$. For frequencies $0 \le \rho \le Delay_1$, native and fringing phase reactions counter-rotate, but require filtering (ρ-dependent weighting) to enhance cancelation of net phase. (b), (c) Conceptually, frequency dependent weights could modify native and fringing peak shapes into green and red triangles, so summed signal (gray rectangle) has constant magnitude and zero phase (dashed gold) independent of Δx. Native must be forced to zero for $Delay_1 < \rho$ since fringing reaction flips polarity at $\rho = Delay_1$, and thus, no opposition occurs for higher frequencies. (c) During equalization another frequency dependent weight is applied to sum (gray) reshaping it to Gaussian (bold magenta) that minimizes ringing in wavenumber ν-space. (d) Optional 2x resolution boosting, using new knowledge of Δx from panel (c) to correct raw data by $-\Delta x$. Because higher frequencies are now present, equalization can be to a Gaussian having ~2x resolution of panel (c).

higher frequency halves of fringing peak are red/blue. For $0 \le \rho \le \text{Delay}_1$, native and fringing phase reactions counter-rotate, but require filtering (ρ-dependent weighting) to enhance cancelation.

Conceptually, any initial lineshape can be reshaped via filtering into (b) simple triangle model (green/red) Sec. 4.2 that demonstrates perfect phase cancellation (dashed gold line) and results in uniform net magnitude (gray box of panel [c]) that explains origin of term "crossfading." A triangle satisfies requirement that native goes to zero for $\text{Delay}_1 < \rho$ (as does sinc function lineshape in Fig. 43 of Ref. 2), required because fringing reaction flips polarity at $\rho = \text{Delay}_1$.

However, in practice, it is not necessary to actually form a triangular shape, because native and fringing ratio is evaluated for each ρ independent of other ρ, and their common value does not matter because it will be modified during equalization step (c). Equalization also corrects any strange ρ-dependent shape that was inadvertently imposed during earlier processes (b). (d) Using new knowledge of Δx from panel (c) to correct raw data by $-\Delta x$, equalization can optionally be to a Gaussian having ~2x resolution of panel (c).

9 Compensating for Glass Dispersion to Linearize the Sine Comb

For a linear phase interpolation between references and science features to be accurate, the interferometer transmission $1 + \cos(2\pi\tau\nu)$ should have a pitch (τ) independent of ν. Interferometer glass elements (etalon and any unbalanced portion of beamsplitter substrate) create slight delay ν dependence due to refractive index. This nonlinearity is measured and its effect removed, so linear interpolation of ϕ versus ν between features is appropriate.

Our calibration compares measured to modeled ThAr moiré phases using library values.[19] Figure 21(a) shows measured E4 delay ν-dependence of T-EDI over 4000 to 11,000 cm^{-1} by phase shift comparison with ThAr emission line model using base delay $\tau_0 = 9676.96$ μm (similar to Sec. 6.5 in Ref. 2). The black curve is 10th order polynomial fit.

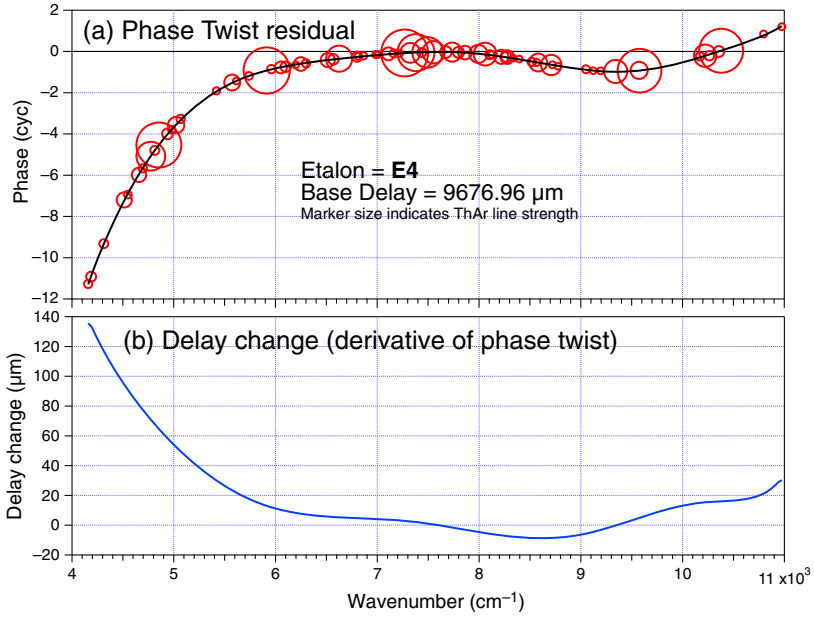

Fig. 21 (a) Measured E4 delay ν-dependence of T-EDI over 4000–11,000 cm^{-1} by phase shift comparison $\theta_{\text{glass}}(\nu)$ with ThAr emission line model[19] using base delay $\tau_0 = 9676.96$ μm. Black curve is 10th order polynomial fit. (b) Derivative $\partial/\partial\nu$ of phase yields effective delay addition [last term Eq. (21)].

9.1 Separating Glass Dispersion From Other Delay Components

The phase can be decomposed into components

$$\phi(\nu) = [\tau_0 + \delta\tau_{ps} + \delta\tau_e] * \nu + \theta_{\text{glass}}(\nu) \tag{20}$$

where τ_0 is base delay, $\delta\tau_{\text{ps}}$ is phase stepping delay (constant during and incremented between exposures), and $\delta\tau_e$ represents unknown environmental drifts (e.g., gravity vector and thermal dilation of mounts), which can slowly change by fraction of a cycle during an exposure and drift more than that between nights. The initial three terms have no significant ν-dependence (except for the multiplication by ν). The ν nonlinearity is lumped into third term $\theta_{\text{glass}}(\nu)$, which is phase twist residual [Fig. 21(a)].

Taking the change in phase per ν derivative of Eq. (20) (in cyc per cm^{-1}) yields for effective delay (cm)

$$\partial\phi(\nu)/\partial\nu = [\tau_0 + \delta\tau_{\text{ps}} + \delta\tau_e] + \partial\theta_{\text{glass}}(\nu)/\partial\nu. \tag{21}$$

Figure 21(b) plots the rightmost term [see Fig. 17(b) of Ref. 2 for dispersion delay addition for etalons E1 through E6]. This glass delay addition varies with ν more broadly than typical spacing ($\sim$75 cm^{-1}) between ThAr reference lines (open circles). Hence, once we remove $\theta_{\text{glass}}(\nu)$, the interferometer phase is linear, and interpolation between reference features to find science features is accurate.

9.2 Linear Interpolation of a Phase Line

Figure 22 plots phase versus ν for a hypothetical science feature S and two nearby reference features R_1 and R_2. The slopes are the delay τ. After the glass dispersion is removed, the phase relation with ν is linear ($\phi = \nu\tau$). The interferometer delay τ can wander a small amount $\delta\tau$ from time A to time B and not harm the determination of the science feature location, bec ause the phase of all the features will shift vertically in a known way, $\delta\phi = \nu\delta\tau$. Linear interpolation between the references and the science feature will still return the same wavenumber ν_s of the science feature. (To remove the effect of the glass dispersion $\theta_{\text{glass}}(\nu)$, we multiply the fringing spectra data $\mathbf{W}(\nu)_{\text{raw}}$ by a complex rotation to form an untwisted fringing spectrum Eq. (5). This linearizes the previously slightly nonlinear data, as if it was made by a constant delay sine comb.)

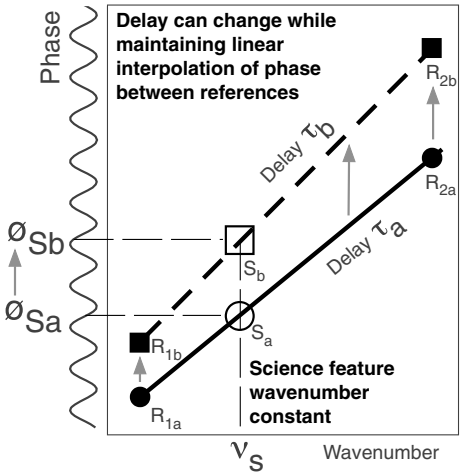

Fig. 22 After glass dispersion is compensated (Sec. 9), delay τ can wander slightly while maintaining linear interpolation of phase between nearby references. Features (reference and science) shift their phase in a mathematically well behaved way ($\phi = \nu\tau$), between two times labeled "a" to "b." Linear interpolation between R_{1b}, S_b, and R_{2b} reveals same position ν_s of science feature despite delay wandering. Note that the sine comb ruler plotted along vertical axis is a mathematical concept and may not manifest a physical comb when spectrum lacks continuum.

10 Background

10.1 Generic Motivation

Spectrographs are used everywhere in science, engineering, medicine, forensics, and remote sensing for national security. Dispersive spectrographs spread the spectrum spatially across a detector and use positional changes to determine wavelength (distance from reference or calibration line). Some spectrographs cannot be perfectly rigid or isothermal, which can cause a wavelength error. This can be corrected by a spectral reference (i.e., ThAr lamp) near to science feature. However, when the reference is too far away from science feature to constrain the wavenumber versus pixel function, an error can persist, which is the case for our TripleSpec data (Fig. 3).

Conventional mitigations such as vacuum tanks, fiber optic scramblers and exquisite thermal control are conventionally used to reduce drifts, but these mitigations can be heavy, expensive, and preclude mobile use on airborne or spaceborne platforms or on the rotating telescope itself due to excessive weight or bulk.

The presence of a dense array of reference features is valuable to combat distortions. A uniform grid of a laser frequency comb (LFC) calibrates those spectrographs able to afford their cost and have sufficiently high resolution to resolve grid spacing. Reference 20 surveys observatory spectrograph performance, and Refs. 21 and 22 describe HARPS performance using a LFC.

For exoplanet Doppler and direct measurement of cosmic redshift drift,[23,24] spectrographs need to be ultrastable—an incredible $1/30,000$ pixel rigidity is needed to characterize an Earth-like planet ($\sim$10 cm/s stability). Cosmic redshift drift measurements require multiyear measurements—a length over which detectors can fail. Replacement detectors can have different pixel placement patterns producing an error. (The EDI's insensitivity to detailed pixel position is an advantage).

10.2 Applications to the Spectroscopic Community

Stellar activity is a nature noise source in the science signal that competes with the apparatus or environmentally caused instrumental noises.[25–29] This may affect spectrograph design tolerance for instrumental drifts in future spectrographs.

Whatever design goal is decided for tolerable instrumental noise, EDI presents a new tool available to designers for achieving their goal while staying within their budget for cost, weight, and bulk. They may decide to reduce cost and performance in of a conventional mitigation, then restore and achieve their net stability goal using EDI. Stability provided by EDI crossfading multiplies, not adds, to conventional mitigations, so combined use is beneficial.

Second, there is a diversity of spectrograph performance levels. Consider a spectrograph at a student observatory. A typical meager budget would not allow conventional mitigations. Yet, it could benefit from lower cost EDI.

Spectrographs used for rotating telescope mounting and airborne remote sensing need both compactness and stability. Compactness is provided by EDI from its resolution boosting[2,3,9,10] ability due to heterodyning. A 10 times resolution boost has been demonstrated (Fig. 22 of Ref. 2). This allows a much more compact and lightweight instrument to reach resolution goals. Second, the same apparatus also provides increased stability through the crossfading data analysis method.

Although EDI is attractive for mobile applications, it is also useful for ultraprecise observatory measurements, because it multiplies rather than adds the sine comb and input spectrum. (Analysis difficulties can result from a constant intensity calibrant compared to a fluctuating input spectrum.) Multiplication guarantees science and comb signals use the same ray paths so they suffer the same distortions. It also provides robustness against variation of detector pixel area.

11 Discussion: Robustness to Wandering Delay

11.1 Interpolate S Between Bracketing *R*

Although interferometer delay stability of monolithic interferometers is welcome, we do not treat our interferometer as an absolute, but as an intermediary bridge, connecting absolute reference

lines to science features measured simultaneously through same interferometer. Anticipated slight wandering of interferometer delay is compensate in data analysis.

Figure 22 shows the spectrograph strategy of externally dispersed interferometry. The R and S symbols represent reference and science (stellar) features, respectively. In some conventional spectrographs, such as in TripleSpec data of Figs. 3 and 4, the focal spot position versus detector pixel is distorted. This creates an error in the perceived wavenumber ν_s for a science feature at position on detector x_s. Figure 22 uses instead a multiplicative sinusoidal comb as a ruler and does not use position on detector to determine fine wavenumber.

The phase of features, R or S, is determined simultaneously in several exposures by ratios of intensities, by dithering the interferometer delay over about a wavelength (called phase stepping). Significantly, the actual detailed period and phase of the multiplicative sine comb does not matter, just the linearity of phase behavior versus ν used to interpolate between nearby reference features. Spectrograph distortions that change focal position and shape affect equally the features and embedded sine comb because they are multiplied together as light passing through interferometer.

11.2 Consequence for Miscalculating Weights

Looking at the simple triangular lineshape model Fig. 10(c) showing the two parabolic reactions (native opposing fringing) that cancel for ideal choice of weights $k_0(\rho) = 1$, $k_1(\rho) = 1$. What is the consequence if a wrong weight is used?

First consider that a 100% reduction of k_1 produces a completely unbalanced reaction, i.e., the same drift Δx as in the disperser used alone, i.e., TRC $= 1$ or $G_{\text{EDI}} = 1$. Thus, a 10% reduction of weights from ideal would cancel 90% of the reaction, leaving 10% undiminished, so TRC $= 0.1$, or $G_{\text{EDI}} = 10$. Because we observe in the actual data TRC $= 0.05$ for a single pass (the slope of Fig. 19), we thus desire the weights to be accurate to 5% or less, to not make the TRC significantly higher than this. Because we are using 6 independent frequency elements to the weight, then if they were uncorrelated and bipolar, we could tolerate individual weight errors of $0.05(\sqrt{6}) = 12\%$ scale.

12 Discussion: Net Stability Is a Product of Conventional and EDI Stabilities

A crossfading EDI used together with conventional mitigations increases the net stability gain (G_{net}) as a product of individual stabilities G_{convent}, G_{EDI},

$$G_{\text{net}} = G_{\text{convent}} G_{\text{EDI}}, \tag{22}$$

where $G \equiv 1/\text{TRC} = \Delta x/\Delta\nu$. This is because conventional mitigations start with an original drift Δx_0 and reduce it $\Delta x = \Delta x_0/G_{\text{convent}}$. By contrast, EDI does not attempt to reduce Δx_0. Instead, it reduces the output spectrum's reaction rate (TRC $= \Delta\nu/\Delta x$) to drift. So, the resulting apparent drift $\Delta\nu$ is smaller

$$\Delta\nu = \Delta x * \text{TRC} = \frac{\Delta x_0}{G_{\text{convent}}} \frac{1}{G_{\text{EDI}}}, \tag{23}$$

and Eq. (22) for G_{net} forms in the denominator.

12.1 Laser Frequency Combs Unresolved by Low Resolution Spectrographs

Current laser frequency comb (LFC) technology cannot be used by low-resolution spectrographs, because they cannot resolve the spacing $\nu_{\text{rep}} = f_{\text{rep}}/c$ between fiducial spikes, having a repetition frequency f_{rep}. For example, the 18 GHz of the HARPS LFC[30] produces a spacing of 18×10^9 sec $^{-1}/(3 \times 10^{10}$ cm sec$^{-1}) = 0.6$ cm^{-1}, which is sufficiently resolved by HARPS, having resolution $R \sim 115,000$ (its PSF at 500 nm (20,000 cm^{-1}) is 0.17 cm^{-1} wide). However, it is not resolved by $R \sim 3000$ resolution of the Triplespec spectrograph at 5000 cm^{-1} (PSF width 1.7 cm^{-1}) or the $R \sim 50$ (100 cm^{-1} PSF) of the Gemini Planet Imager integral field spectrograph.[31,32]

13 Concluding Remarks

Theoretically, studying the EDI behavior to a disperser drift, especially in Fourier space, leads to a powerful insight: fringing frequencies lower than the delay (interferometer comb frequency) move oppositely in phase to those of the ordinary native spectrum.

This leads us to a new data analysis algorithm (crossfading or X-EDI) that combines native and fringing signals after strategic filtering. The frequency dependent weights are chosen to cancel the phase shift due to drift Δx. This method is an extension of a prior demonstrated crossfading algorithm using pairs of delays. In the present paper, we substitute the native for the lower delay, and the single delay for the upper delay, of the earlier crossfading method.[14]

Simulations (Figs. 12, 17, and 19) confirm that the X-EDI algorithm produces about a 20 times reduction of reaction to a drift Δx, for a single pass. Application of the crossfading on real data from four stellar spectra having four independent drifts (Fig. 11) is also successful.

Iterative application of the algorithm improves stability dramatically more. The opposition of the lower fringing frequencies is a strong negative feedback signal useful in a conceptual control loop to converge rapidly to a stable spectrum and yield Δx. Starting from a 0.5 cm^{-1} drift [31 km/s Doppler equivalent], seven iterations reduces the reaction down to 4×10^{-7} cm^{-1} [2.5 cm/s], which is about an order of magnitude per iteration. This result is preliminary because the algorithm has not yet been experimentally tested at the centimeter per second level.

This work shows promise for some spectroscopic applications where spectral calibration lines are sparse. Spectrograph designers may find it useful to have another avenue for high spectral resolution with a more mathematically simple and uniform PSF that interferometry provides that can tolerate sparser density of calibration features while having less weight or bulk or expense.

13.1 Impact for Remote Sensing Mobile Platforms

Mobile platforms, such as airborne platforms, would especially benefit. These cannot tolerate the large weight and bulk of a vacuum tank and thermal insulation. Using EDI thus provides a way of dramatically reducing the effect of wavelength drift errors due to accelerations, vibration, and barometric and thermal changes. The cost of EDI is some flux loss at the additional optical interfaces of the interferometer and more complicated software to interpret the data.

13.2 Effective Spectral Resolution Can Be Doubled

An additional benefit of X-EDI, although not the focus of this paper, is that the effective spectral resolution of the disperser can be doubled or more without changing the disperser slit width or grating.[2,9,10] This is due to the heterodyning action which occurs because the input spectrum is multiplied by a sinusoid, which shifts high frequencies down to lower frequencies, which are more resolvable by the native spectrograph and detector.

13.3 Comparison to Conventional Algorithms

Our project funding ended in October 2023; the crossfading code is in a preliminary state. Code has not yet been written to compute data over full TripleSpec echelle bandwidth over which optimal crossfading weights slowly change. However, we can compare with conventional behavior for small bandwidths. Figure 19 shows a slope of 1/20, so the EDI method would be 20x better than conventional for a single pass. Iterating the crossfading produces successively smaller error, and 10^6 stability gain was achieved in six iterations.

The EDI strategy for improving wavelength stability is to decouple the detailed position on detector from the wavelength determination. The disperser has detector position dependence, whereas interferometry measures fine wavelength by intensity ratios, which measure fringe phase, which in turn determines wavelength.

14 Appendix A: Comparing Crossfading EDI to a Stable Monolithic Interferometer

It is useful to compare/contrast crossfading-EDI (X-EDI) with the stable monolithic interferometer (SMI)[33–37] of Fig. 4 of article,[35] used in MARVELS (Multi-object Apache Point Observatory Radial Velocity Exoplanet Large-area Survey of Sloan Digital Sky Survey).[38] Table 2 lists at least

Table 2 Distinctions between the two ideas (method improvements) of (SMI) stable monolithic interferometer and (X-EDI) crossfading externally dispersed interferometry. See Table 3 for places where the two methods or philosophies agree. This table mainly list contrasts, to aid the reader in distinguishing the methods.

Note#	Question	SMI	X-EDI
1	Kind of Advance	Hardware	Data Analysis Math
2	Stabilize what?	Interferometer	Disperser
3	How many interferometers?	1 or 2	1
4a	Type sine comb ruler?	Additive	Multiplicative
4b	Heterodyning of stellar spectrum?	Only in EDI portion	Yes
4c	Physical comb ruler?	Yes, lamp photons	No, is math concept
4d	Darkness between ThAr lamp lines?	No, a comb is present	Yes, darkness
5	Interferometer stability needed?	Yes	Nice but not needed
6	Theory of how disperser wavelength drift affects fringe?	No	Yes
7	Recognition of opposition in high and low fringe freq. behavior?	No	Yes
8	Data analysis filters out frequencies higher than delay?	No	Yes
9	Data analysis sums strategically filtered native and fringing?	No	Yes
10	2x resolution boosting option?	No	Yes
11	Apply retroactively to older EDI data?	No	Yes

Table 3 Commonalities between the two ideas of (SMI) stable monolithic interferometer and (X-EDI) crossfading externally dispersed interferometry. See Table 2 for places where the two methods disagree.

Note#	Issue	SMI	X-EDI
a	Trust interferometer behavior over disperser	Yes	Yes
b	EDI portion used to analyze spectrum	Yes	Yes
c	Absolute calibration provided spectroscopically	Yes	Yes

11 distinctions. Table 3 lists commonalities, notably, both use the EDI method[5,39] to analyze a spectrum.

Distinctions include SMI stabilizing the interferometer, whereas X-EDI stabilizes the disperser. SMI is a hardware advance, and X-EDI is a data analysis advance. The SMI white light comb (WLC) is an additive sine comb, whereas EDI uses a multiplicative sine comb (which enables heterodyning and thus a resolution boost). T-EDI used a single interferometer to measure starlight $S(\nu)$ and additive ThAr lamp $\mathrm{ThAr}(\nu)$

$$S_{\mathrm{tedi}}(\nu) = [S(\nu) + \mathrm{ThAr}(\nu)]T_{\mathrm{edi}}(\nu), \tag{24}$$

by multiplying against sine comb $T_{\mathrm{edi}}(\nu)$, which is Eq. (1) with delay τ_1. A distinction from SMI is X-EDI does not use an additive WLC, as proven by lack of comb in darkness inbetween ThAr lines in data (Fig. 13).

By contrast, SMI instrument MARVELS (Fig. 4 of Ref. 35) has two interferometers (WLC and EDI) described by

$$S_{\text{marvels}}(\nu) = [\text{WLC}(\nu) + S(\nu) + \text{ThAr}(\nu)]T_{\text{edi}}(\nu), \tag{25}$$

where $\text{WLC}(\nu) = \text{Lmp}(0.5)(1 + \cos 2\pi\nu\tau_L)$ with (Lmp) lamp intensity and WLC delay τ_L. A key idea of SMI is to make WLC stable, to make it attractive as a calibration source. However, because $\text{WLC}(\nu)$ is an emission source, it does not multiply $S(\nu)$. Hence, it does not heterodyne the stellar spectrum. However, $S(\nu)$ does multiply with MARVELS downstream EDI sinusoid $T_{\text{edi}}(\nu)$.

Heterodyning is necessary for resolution boosting[2,5,9,10] (and the negative feedback used in crossfading). Resolution boosting makes an EDI attractive. Crossfading makes EDI even more attractive with (effectively) increased disperser stability.

The SMI technique can stabilize an EDI delay. Although that is welcome, we find it unnecessary, because we calibrate the EDI delay spectroscopically using ThAr spectral lines taken simultaneously with data. Using a spectral reference is necessary even if the delay was stabilized, because we command delay increments ($\sim\lambda/4$) with PZT voltage changes to create phase stepping exposures. These voltage steps are imprecise to the extreme level needed for low mass exoplanet Doppler velocimetry. The solution is that software measuring stellar fringe phase also measures reference ThAr phase. The stellar phase minus ThAr phase [Eq. (13)] yields the science Doppler value. This effectively removes the detailed value of the delay from the Doppler measurement, because both stellar and ThAr phases are drifted by the same amount.

Although this subtraction addresses drifts in delay, what about wavelength drifts in the disperser? For an arbitrary spectrum having arbitrary FT distribution (against the inclined phase error line in Fig. 7), there is a potential for unbalanced phase error—we developed crossfading to mitigate this (blue line in Fig. 9). A US patent 12,480,815 describing single-delay crossfading EDI has issued Nov. 25, 2025, to Lawrence Livermore National Security with the first author as inventor.[40]

14.1 Table 2 Notes on Distinctions

[Notes 1, 2] SMI improves interferometer hardware to stabilize delay drifts; X-EDI improves EDI data processing to stabilize disperser drifts. **[Note 3]** SMI: either one interferometer as an EDI (Fig. 1 of Ref. 34) or two when a 2nd one makes a WLC for that EDI (Fig. 4 of Ref. 35).

[Note 4a] SMI: Additive when its makes a WLC; multiplicative when used as EDI. EDI or X-EDI: starlight or ThAr passes through interferometer and is multiplied by sine comb. **[Note 4b]** Eq. (25) shows additive comb $\text{WLC}(\nu)$ and input spectrum $S(\nu)$ do not multiply each other, hence do not heterodyne. However, $S(\nu)$ does multiply with the EDI sinusoid $T_{\text{edi}}(\nu)$. **[Notes 4c, d]** X-EDI: the $T_{\text{edi}}(\nu)$ multiplies input spectrum. If this has zero intensity in regions, zero photons are detected. SIM: if WLC is used, lamp photons are detected even in regions where no input spectral photons exist. Our data (Fig. 13) show darkness in between ThAr lamp lines (WLC $= 0$ and $S = 0$) proving lack of additive sine comb.

[Note 5] SMI: delay stability is their goal. X-EDI: stable delay is nice, but since it is calibrated via two spectral lines it can wander. **[Note 6]** X-EDI: we mathematically describe how disperser drift effects fringe phase. **[Note 7]** This key observation is central to our algorithm. **[Note 8]** Only frequencies less than delay react to Δx in opposition. **[Note 9]** X-EDI: native and fringing signals are first filtered, then summed. **[Note 10]** X-EDI: native and fringing can be combined to boost resolution $\sim 2x^9$ (Fig. 18). SMI: additive WLC does not multiply against stellar $S(\nu)$ and thus cannot boost resolution. **[Note 11]** Our present paper re-analyzes EDI data taken in a 2007–2011 project.

14.2 Table 3 Notes on Commonalities

[Note A] Both teams believe that interferometer PSF has fewer degrees of freedom than disperser PSF. **[Note B]** Their term [Dispersed] Fixed Delay Interferometer for 2nd interferometer in MARVELS (Fig. 4 of Ref. 35) is linked to our term externally dispersed interferometer[y], and earlier term Fringing Spectrometer, by Jian Ge's 2003 errata.[39] A patent[5] describing EDI by inventor David J. Erskine issued February 26, 2002. This useful for priority, although more than

20 years old and in the public domain. **[Note C]** In SMI-MARVELS, ThAr lamp calibrates WLC. X-EDI: delay calibrated by ThAr lamp recorded simultaneous to stellar.

15 Appendix B: Temperature Induced Wandering of Delay

15.1 Actual T-EDI Drift

The T-EDI interferometer was located in the Hale telescope Cassegrain hole surrounded by massive 5-m mirror, naturally producing a thermally stable environment. Ten phase step exposures per delay took ~5 min, and random scatter in ThAr reference was very small at $\delta\tau_e = 0.006$ μm (Fig. 10(b) of Ref. 2). By contrast, the conventional spectrograph (TripleSpec[4]) suffered significant drifts (Fig. 3). This was mounted outside the Cassegrain cavity inside a liquid nitrogen jacket.

15.2 Hypothetical Drift if in Different Environment

References 33–37 describe thermally stable monolithic interferometers (SMI), using two glasses (BK7 and LAK7) having different thermal responses to cancel net drift.

T-EDI was not monolithic. This was to allow delay selection of free standing etalons (fused silica). Malitson[41] measured fused silica dn/dT of $\sim 11 \times 10^{-6}$ per °C at 1 μm and Hahn[42] the coefficient of thermal expansion (CTE) as 0.5×10^{-6}, but the dn/dT dominates, yielding ~0.1 cycle phase shift per °C. Thermal delay drifts are a "piston" component $\delta\tau_e$ affecting all ν plus a ν-dependent residual measured and compensated by a phase twist residual analogous to $\theta_{\text{glass}}(\nu)$.

Note that short term thermal delay wandering would be much smaller than the ~1 cycle commanded phase shift via PZT transducer (over a dataset of 5 min); hence, the stable delay of SMI was not required for T-EDI. (For long term, it would have been convenient, but still not required, because the absolute delay was measured spectroscopically via ThAr.)

Disclosures

The authors have no conflicts of interests.

Code and Data Availability

The data presented in this article are not publicly available. If you require these data, contact the corresponding author at derskine@spectralfringe.org.

Acknowledgments

Thanks for help with the TEDI project on Mt. Palomar Observatory from many colleagues, including James Lloyd, Phil Muirhead and Matthew Muterspaugh. Thanks to late John R. Erskine and Neil C. Holmes for early mentoring and scientific/natural inspiration, Ed I. Moses, Steve Libby, D. Rotman, E. K. Wheeler, L. L. LoDestro and O. Pearce for getting the ball rolling, guidance from Richard Ozer of the Eastbay Astronomical Society. Thanks to Emma Floyd for recent discussions on fringe whispering. High-resolution spectra of a ThAr lamp provided by Florian Kerber (NIST). This work performed under the auspices of the U.S. Department of Energy by Lawrence Livermore National Laboratory under Contract DE-AC52-07NA27344. Work supported by Laboratory Directed Research and Development project 22-LW-020, and based upon prior work supported by the National Science Foundation under Grant Nos. AST-0505366, AST-096064, PAARE AST-1059158, and NASA Grant NNX09AB38G.

References

1. P. S. Muirhead et al., "Precise stellar radial velocities of an M Dwarf with a Michelson interferometer and a medium-resolution near-infrared spectrograph," *Publ. Astron. Soc. Pac.* **123**, 709–724 (2011).
2. D. J. Erskine et al., "High-resolution broadband spectroscopy using externally dispersed interferometry at the Hale Telescope: part 1, data analysis and results," *J. Astron. Telesc. Instrum. Syst.* **2**, 025004 (2016).
3. D. J. Erskine et al., "High-resolution broadband spectroscopy using externally dispersed interferometry at the Hale Telescope: part 2, photon noise theory," *J. Astron. Telesc. Instrum. Syst.* **2**, 045001 (2016).
4. J. C. Wilson et al., "Mass producing an efficient NIR spectrograph," *Proc. SPIE* **5492**, 1295–1305 (2004).

5. D. J. Erskine, "Combined dispersive/interference spectroscopy for producing a vector spectrum," US Patent 6,351,307 (2002).
6. D. J. Erskine and J. Ge, "Novel interferometer spectrometer for sensitive stellar radial velocimetry," *ASP Conf. Ser.* **195**, 501–507 (2000).,
7. J. Ge, D. J. Erskine, and M. Rushford, "An externally dispersed interferometer for sensitive Doppler extrasolar planet searches," *Publ. Astron. Soc. Pac.* **114**, 1016–1028 (2002).
8. D. J. Erskine, "An externally dispersed interferometer prototype for sensitive radial velocimetry: theory and demonstration on sunlight," *Publ. Astron. Soc. Pac.* **115**, 255–269 (2003).
9. D. J. Erskine et al., "High-resolution broadband spectroscopy using an externally dispersed interferometer," *Astrophys. J.* **592**, L103–L106 (2003).
10. D. J. Erskine and J. Edelstein, "Interferometric resolution boosting for spectrographs," *Proc. SPIE* **5492**, 190–199 (2004).
11. D. J. Erskine et al., "Noise studies of externally dispersed interferometry for Doppler velocimetry," *Proc. SPIE* **6269**, 62692P (2006).
12. D. J. Erskine et al., "Enhanced exoplanet biosignature detection from an interferometer addition to low resolution spectrographs," *Proc. SPIE* **10702**, 107024G (2018).
13. D. J. Erskine, "Dispersed interferometers," in *The WSPC Handbook of Astronomical Instrumentation*, D. N. Burrows, Ed., Vol. **3**, World Scientific, Singapore (2021).
14. D. J. Erskine, "Method for boosting dispersive spectrograph stability, 1000x, using interferometry with cross-faded pairs of delays," *J. Astron. Telesc. Instrum. Syst.* **7**, 025006 (2021).
15. J. Ge et al., "The first extrasolar planet discovered with a new-generation high-throughput doppler instrument," *Astrophys. J.* **648**, 683–695 (2006).
16. B. Ma et al., "Very low-mass stellar and substellar companions to solar-like stars from MARVELS. VI. a giant planet and a brown dwarf candidate in a close binary system HD 87646," *Astron. J.* **152**, 112 (2016).
17. J. C. van Eyken, J. Ge, and S. Mahadevan, "Theory of dispersed fixed-delay interferometry for radial velocity exoplanet searches," *Astrphys. J. Suppl. Ser.* **189**, 156–180 (2010).
18. J. C. van Eyken et al., "First planet confirmation with a dispersed fixed-delay interferometer," *Astrophys. J.* **600**, L79–L82 (2004).
19. F. Kerber, G. Nave, and C. J. Sansonetti, "The spectrum of th-ar hollow cathode lamps in the 691-5804 nm region: establishing wavelength standards for the calibration of infrared spectrographs," *Astrophys. J. Suppl. Ser.* **178**, 374–381 (2008).
20. D. A. Fischer et al., "State of the field: extreme precision radial velocities," *Publ. Astron. Soc. Pac.* **128**, 066001 (2016).
21. D. Milaković and P. Jethwa, "A new method for instrumental profile reconstruction of high-resolution spectrographs," *Astron. Astrophys.* **684**, A38 (2024).
22. D. Milaković et al., "Precision and consistency of astrocombs," *Mon. Not. R. Astron. Soc.* **493**, 3997–4011 (2020).
23. A. G. Kim et al., "Giving cosmic redshift drift a whirl," *Astropart. Phys.* **62**, 195–205 (2015).
24. D. Erskine et al., "Direct acceleration: cosmic and exoplanet synergies, Bull," *Am. Astron. Soc* **51**, 53 (2019).
25. A. A. John et al., "Sub-m s-1 upper limits from a deep HARPS-N radial-velocity search for planets orbiting HD166620 and HD144579," *Mon. Not. R. Astron. Soc.* **525**, 1687–1704 (2023).
26. L. L. Zhao et al., "The expres stellar signals project II. State of the field in disentangling photospheric velocities," *Astron. J.* **163**, 171 (2022).
27. L. L. Zhao et al., "The extreme stellar-signals project," *Astron. J.* **166**, 173 (2023).
28. Y. Zhao et al., "Improving Earth-like planet detection in radial velocity using deep learning," *Astron. Astrophys.* **687**, A281 (2024).
29. B. Klein et al., "Investigating stellar activity through eight years of sun-as-a-star observations," *Mon. Not. R. Astron. Soc.* **531**, 4238–4262 (2024).
30. G. L. Curto et al., "Achieving a few cm/sec calibration repeatability for high resolution spectrographs: the laser frequency comb on HARPS," *Proc. SPIE* **8446**, 84461W (2012).
31. B. A. Macintosh et al., "The Gemini Planet Imager: from science to design to construction," *Proc. SPIE* **7015**, 701518 (2008).
32. S. G. Wolff et al., "Gemini planet imager observational calibration XIII: wavelength calibration improvements, stability, and nonlinearity," *Proc. SPIE* **9908**, 990838 (2016).
33. X. Wan and J. Ge, "Monolithic Michelson Interferometer as ultra stable wavelength reference," *Proc. SPIE* **7734**, 77343N (2010).
34. X. Wan, J. Ge, and Z. Chen, "Development of stable monolithic wide-field michelson interferometers," *Appl. Opt* **50**, 4105–4114 (2011).
35. J. Wang et al., "Accurate group delay measurement for radial velocity instruments using the dispersed fixed delay interferometer method. II. Application of heterodyne combs using an external interferometer filter," *Pub. Astron. Soc. Pac.* **124**, 1159–1166 (2012).

36. S. Mahadevan et al., "An inexpensive field-widened monolithic michelson interferometer for precision radial velocity measurements," *Publ. Astron. Soc. Pac.* **120**, 1001–1015 (2008).
37. X. Wan and J. Ge, "Stable monolithic interferometer for wavelength calibration," US Patent 8,570,524 (2013).
38. J. Ge et al., "A new generation multi-object Doppler instrument for the SDSS-III multi-object apo radial velocity exoplanet large-area survey," *Proc. SPIE* **7440**, 74400L (2009).
39. J. Ge, "Erratum: fixed delay interferometry for Doppler Extrasolar Planet Detection," *Astrophys. J.* **593**, L147 (2003).
40. D. J. Erskine, "Spectrograph stabilization using a single-delay interferometer," US Patent 12,480,815 (2025).
41. I. H. Malitson, "Interspecimen comparison of the refractive index of fused silica," *J. Opt. Soc. Am.* **55**, 1205–1209 (1965).,
42. T. A. Hahn and R. K. Kirby, "Thermal expansion of fused silica from 80 to 1000 K standard reference material 739," *AIP Conf. Proc.* **3**, 13–24 (1972).

David J. Erskine received his PhD from Cornell in 1984. He has been an experimental physicist at Lawrence Livermore National Laboratory with experience in femtosecond lasers, semiconductor physics, superconductivity, diamond anvil cell high pressure physics, shock physics, high-speed recording techniques, Doppler interferometry, white light interferometry, digital holography, Fourier signal processing, image reconstruction, and phase stepping algorithms for interferogram analysis. He collaborates with astronomers on interferometric techniques for the Doppler planet search and high-resolution spectroscopy. He is a member of SPIE.

Biographies of the other authors are not available.